Am J Physiol Cell Physiol 330: C1460–C1473, 2026.
First published April 1, 2026; doi:10.1152/ajpcell.00838.2025

american physiological society

AMERICAN JOURNAL OF PHYSIOLOGY
CELL PHYSIOLOGY

RESEARCH ARTICLE

Fibroblast specialization across microanatomy in a single-cell atlas of human Achilles tendon

Carla J. Cohen,[1,2]* Jolet Y. Mimpen,[1,3]* Alina Kurjan,[1] Claudia Paul,[1] Shreeya Sharma,[1] Lorenzo Ramos-Mucci,[1] Chinemerem T. Ikwuanusi,[1] Ali Cenk Aksu,[1] Tracy Boakye Serebour,[1] Marina Nikolic,[1] Kevin Rue-Albrecht,[2] Christopher Gibbons,[1] Duncan Whitwell,[1] Tom Cosker,[1] Steven Gwilym,[1] Ather Siddiqi,[1] Raja Bhaskara Rajasekaran,[1] Harriet Branford-White,[1] Adam P. Cribbs,[1] Philippa A. Hulley,[1] David Sims,[2] Mathew J. Baldwin,[1]* and Sarah J. B. Snelling[1]*

[1]*The Botnar Institute of Musculoskeletal Sciences, Nuffield Department of Orthopaedics Rheumatology and Musculoskeletal Sciences, University of Oxford, Oxford, United Kingdom;* [2]*Centre for Computational Biology, MRC Weatherall Institute of Molecular Medicine, University of Oxford, Oxford, United Kingdom; and* [3]*Kennedy Institute of Rheumatology, Nuffield Department of Orthopaedics Rheumatology and Musculoskeletal Sciences, University of Oxford, Oxford, United Kingdom*

Abstract

Tendons are transitional tissues linking muscle to bone, enabling locomotion and fine motor control. The cellular biology across the Achilles tendon unit is poorly understood, yet is critical for interpreting normal function and pathological changes across its microanatomically defined functional zones. We generated a spatially resolved transcriptomic atlas of adult (age 45–76) nontendinopathic human Achilles tendon, sampling the tendon-bone junction (enthesis), midbody, myotendinous junction, and adjoining muscle. Six fibroblast subtypes were identified, with distinct transcriptional profiles and spatial distributions, suggesting specialized functional roles across the tendon. Two dominant fibroblast types were specifically positioned in the tendon midsubstance and paratenon (vessel-rich region surrounding the tendon fibrils); other populations included perineural, myotendinous junction-specific, muscle-specific, and lining-layer fibroblasts. These findings demonstrate how cellular diversity across a transitional tissue may underlie microanatomical-specific roles. This atlas provides a foundation for understanding cellular functions across the tendon and adjoining muscle and will be essential for comparisons with diseased tissue, identifying pathogenic mediators and treatment targets for autoimmune and degenerative pathologies of the Achilles tendon.

NEW & NOTEWORTHY We present the first spatially resolved single-cell atlas of the human Achilles tendon. By sampling across the microanatomy of the tendon from enthesis to muscle, we demonstrate changes in fibroblast composition across this transitional tissue. Distinct fibroblast subsets were discovered with specific transcriptomic signatures, and several were found in distinct spatial locations corresponding to putative functional roles in tendon and adjoining muscle. These findings demonstrate how cellular diversity across a transitional tissue may underlie microanatomical-specific roles.

fibroblast; spatial transcriptomics; tendon; transcriptomics

INTRODUCTION

The Achilles tendon is the largest in the human body. It is an energy-storing tendon and is crucial for mobility, transferring mechanical forces through linking the calcaneal bone of the ankle to the gastrocnemius and soleus muscles of the lower leg (1). Tendon, muscle, and bone are classically regarded as distinct tissue types with unique cell types and functions. However, tendons transition through microanatomical zones with specific biological and mechanical requirements, particularly at bone (enthesis) and muscle (myotendinous) junctions (Fig. 1). At a cellular level, these microanatomies are likely to require different resident cell types and relative cellular compositions to maintain tendon health in response to normal loading and to orchestrate the response to injury and disease (2). Achilles tendon ruptures are the most common tendon injury of the lower extremities, and predominantly occur in the midbody of the tendon, but also rarely at the myotendinous junction (MTJ) and enthesis (3–5). The Achilles can also be affected by enthesopathies, inflammation of the enthesis, including ankylosing spondylitis and psoriatic arthritis (6). A deeper understanding of the transitional tendon microanatomy in health, and in particular, the specific cellular composition of each zone, is needed to understand its contribution to normal mechanical processes and in disease (7).

Histologically, the normal midbody tendon consists of collagen I-rich fibrils that tightly pack to form parallel bundles

*C. J. Cohen and J. Y. Mimpen contributed equally to this work. M. J. Baldwin and S. J. B. Snelling contributed equally to this work.
Correspondence: C. J. Cohen (carla.cohen@ndorms.ox.ac.uk).
Submitted 12 November 2025 / Revised 3 December 2025 / Accepted 26 March 2026

0363-6143/26 Copyright © 2026 The Authors. Licensed under Creative Commons Attribution CC-BY 4.0.
Published by the American Physiological Society.

Downloaded from journals.physiology.org/journal/ajpcell (090.211.155.175) on May 11, 2026.

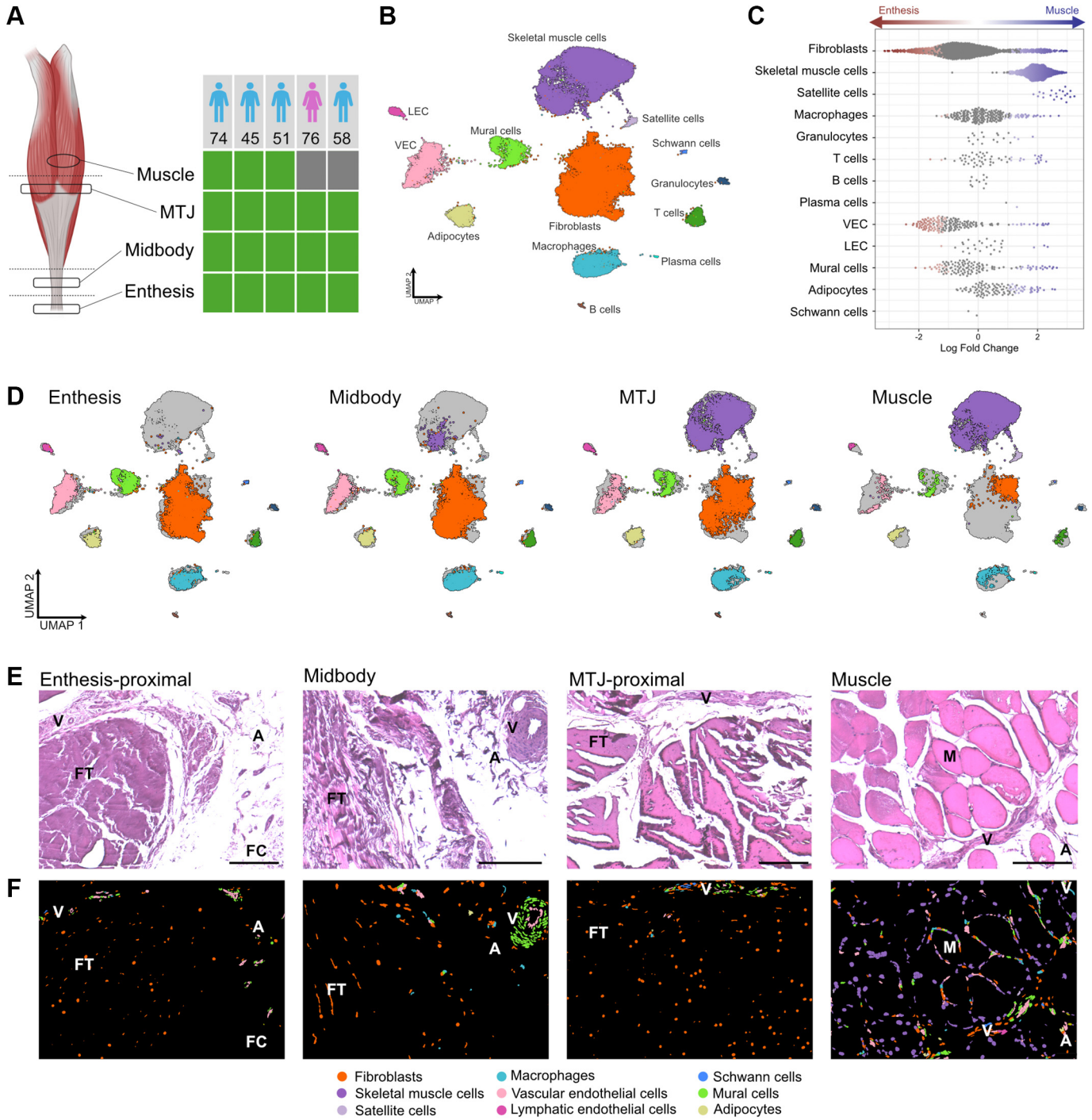


Figure 1. Cell composition varies considerably across Achilles tendon microanatomy. *A*: schematic of the lower leg and human Achilles tendon showing tissue regions sectioned for single-nucleus RNA-seq, spatial transcriptomics, and imaging at three Achilles tendon microanatomies (enthesis-proximal, midbody, and MTJ-proximal) and adjoining muscle. Table shows sample inclusion, sex, and age of participants ($n = 5$). *B*: UMAP representation of broad cell types found in Achilles tendon and adjoining muscle using snRNA-seq. *C*: beeswarm plot showing differential abundance of each broad cell type across microanatomy calculated using MiloR. Each dot represents one cellular neighborhood comprising tens to hundreds of similar cells; red and blue colors indicate neighborhoods with significantly greater abundance at the enthesis or muscle, respectively. *D*: UMAP representation of broad cell types showing cells present at each microanatomy (same colors as *B*). *E*: post-Xenium H&E images from each microanatomy ($n = 1$). *F*: representative spatial transcriptomics plots from each microanatomy ($n = 1$). Broad cell annotations were predicted from the snRNA-seq data; colors as in *B*. Scale bar: 250 μm. A, adipose tissue; FC, fibrocartilage; FT, fascicular tendon; M, muscle; V, vessel. Figure created with a licensed version of BioRender.com.

Downloaded from journals.physiology.org/journal/ajpcell (090.211.155.175) on May 11, 2026.

or fascicles (2, 8). The major cell type within this region is typically regarded to be "tenocytes"—fibroblasts that produce and turnover the extracellular matrix that comprises the bulk of tendon tissue. Collagen fascicles are surrounded by an interfascicular matrix (also referred to as endotenon), which acts as a conduit for nerve, blood, and lymphatic vessels, and is an extension of the epitenon and paratenon (together called peritendon) that surrounds the tendon body (1, 9). Toward the MTJ, skeletal muscle fibers and collagen I fibrils are seen to interdigitate, with ridge-like protrusions of tendon into furrow-like muscle indentations, greatly maximizing surface area and ensuring strong connections between the tendon and muscle tissue (10, 11). Within the enthesis region, collagen fiber alignment decreases, collagen II and proteoglycan levels increase, as does mineralization status, with chondrocyte-like cells also present (12). These transitions across tendon microanatomy enable effective force transfer between muscle and bone.

Single-cell and spatial transcriptomic studies have identified functional tissue niches comprising specific cellular compartments, for example, in the gut and kidney (13, 14). The complexity of tendon cellular composition has been revealed by recent single-cell studies of human hamstring, quadriceps and supraspinatus, and developmental tendons (15–25). Although fibroblasts remain the predominant cell type in these tendons, distinct fibroblast subtypes were also identified, alongside endothelial cells, immune cells, adipocytes, and nervous system cells. Comparison with diseased tissue highlighted alterations in cell activation states in tendon tears (22, 25). Single-cell transcriptomic analysis of Achilles tendon in 6-wk-old mice also described fibroblast, endothelial, and immune populations (26). However, a detailed analysis of the human Achilles tendon, with its unique energy-storing properties, and the relation of cells to their spatial position within tendon microanatomy remains absent.

Therefore, we aimed to use single-nucleus RNA sequencing and spatial transcriptomics on human nontendinopathic Achilles tendon to identify the specific cell types present across the tendon enthesis, midbody, MTJ, and adjacent muscle. These data will enable insights in the compositional and transcriptional changes across the length of the Achilles tendon and will form a valuable reference dataset for future comparative studies on the cellular pathogenesis of Achilles tendon and regenerative medicine approaches targeting the Achilles tendon.

MATERIALS AND METHODS

Ethics

Ethical approval was granted for the Oxford Musculoskeletal Biobank (19/SC/0134) by the local research ethics committee (Oxford Research Ethics Committee B) for all work on Achilles tendon, and informed written consent was obtained from all patients according to the Declaration of Helsinki.

Tissue Acquisition and Processing

Achilles tendon tissue was collected from patients undergoing above-the-knee lower leg amputation due to nonreconstructable sarcoma. Patients were excluded from the study if they had an active infection at the time of surgery or were not weight-bearing. The age, sex, and affected side of the donors are reported alongside the de-identified study ID of each patient (Table 1). Tendon tissue was processed as previously described (27). Briefly, tissue was collected in cold DMEM-F12 media (Gibco) supplemented with 10% fetal bovine serum (Labtech International) and 1% penicillin/streptomycin (Gibco). The collected sample was processed within 2 h of tissue collection. Tendon was washed in PBS, fat and muscle were dissected off, and the tendon was cut into 1-cm tissue strips from the enthesis to MTJ; the 1-cm wide tissue strips were then cut into 1-cm pieces. Tissue pieces representing the enthesis (piece nearest bone), midbody (at narrowest point), and MTJ (wider point nearest muscle) were selected for processing from five patients, and adjoining muscle tissue (triceps surae) was collected from three patients (Table 1 and Fig. 1*A*). Tissues were photographed to retain topographical reference. Adjoining muscle tissue (triceps surae) was collected from three patients (Table 1). The pieces of tendon and muscle tissue were snap-frozen in cryotubes using liquid nitrogen and stored at −80°C until use. Some pieces of tendon and muscle were fixed by immersing the tissues in 10% formalin for 1–2 days (accounting for a penetration rate of ∼0.5 mm/h) at room temperature, washed, and transferred to 70% industrial methylated spirit (IMS) for short-term storage at 4°C until wax embedding.

H&E Imaging

Paraffin-embedded Achilles samples were sectioned at a thickness of 5 µm, deparaffinized, and rehydrated. They were incubated with Gill's III Hematoxylin (Sigma-Aldrich) for 8 min, blued with 0.1% sodium bicarbonate solution for 30 s, and differentiated with 0.3% acid alcohol for 30 s. The sections were then stained with 0.5% aqueous eosin Y solution (Sigma-Aldrich), acidified with glacial acetic acid for 5 min, and the excess stain was washed off. The slides were then dehydrated, mounted with DPX (Sigma-Aldrich), and imaged with the MoticEasyScan One digital slide scanner (RRID:SCR_024855).

Single-Nucleus RNA Sequencing

Nuclei isolation.

Nuclei were isolated from the snap-frozen tissue pieces weighing 0.23–0.44g (similar weight was used for each microanatomical region of each patient) using our previously published protocol (28). In short, the Achilles tendon was cut into thin sections (from tendon tissue from proximal to enthesis, midbody, or proximal to the MTJ) using a

Table 1. *Summary of patient demographics, including de-identified patient ID, sex, age (in years), affected side, and whether muscle was collected*

Patient ID	Sex	Age, yr	Affected Side	Muscle Collected
MSK0785	Male	74	Left	Yes
MSK1250	Male	45	Left	Yes
MSK1556	Male	51	Right	Yes
MSK1687	Female	76	Left	No
MSK1691	Male	58	Right	No

Downloaded from journals.physiology.org/journal/ajpcell (090.211.155.175) on May 11, 2026.

scalpel, forceps, and a petri dish that were all precooled on dry ice and stored in a 50 mL Falcon tube at −80°C until use. Adjacent triceps surae muscle was cut similarly. On the day of cell lysis, the tubes containing the cut tissue were thawed, and 4 mL of cold 1X CST buffer [containing NaCl, Tris-HCl pH 7.5, $CaCl_2$, and $MgCl_2$, with CHAPS hydrate (Sigma), BSA (Sigma), RNase inhibitors (RNaseIn Plus; Promega and SUPERase In; Invitrogen), and protease inhibitor (cOmplete tablet; Roche); full recipe can be found in the published protocol] was added. After 10 min of incubation on a rotor at 4°C, the tissue/buffer mixture was poured through a 40-μm strainer and the tube used for tissue lysis was washed twice with 2 mL PBS with 1% BSA. The nuclei solution was then transferred to a 15 mL Falcon tube, and the previous 50 mL tube was washed once with 4 mL PBS with 1% BSA and transferred to the same 15 mL Falcon tube. The nuclei solution was centrifuged at 500 *g* at 4°C for 5 min. After pouring off the supernatant, the tubes were briefly spun down, the nuclei were resuspended in the supernatant, and the remaining volume was determined. The concentration of nuclei was determined by counting DAPI-stained nuclei in a Neubauer Improved hemocytometer (NanoEnTek).

Library preparation and sequencing.

Nuclei suspensions were diluted (PBS with 1% BSA) to 860–1,000 nuclei/μL and loaded onto the 10X Genomics Chromium Controller Genetic Analyzer (RRID:SCR_019326), then libraries were prepared using the Chromium Next GEM Single Cell 3′ Reagent Kits v3.1 (10x Genomics), following the manufacturer's instructions, and indexed with the Single Index Kit T Set A (10x Genomics). Quality control of cDNA and final libraries was analyzed using High Sensitivity ScreenTape assays on Agilent 4150 TapeStation System (RRID:SCR_019393). Final libraries were pooled and sequenced on an Illumina NovaSeq 6000 Sequencing System (RRID:SCR_016387) by Azenta Life Sciences at a minimum depth of ∼20,000 read pairs per expected nuclei.

Single-Nucleus RNA Sequencing Data Analysis

Quality control and filtering.

Raw NGS data were quality controlled and mapped using the *scflow quantnuclei* pipeline (https://github.com/cribbslab/scflow; python v3.8.15). Specifically, quality control of Fastq files was performed using fastqc (v0.12.1). Fastq files were mapped to the human Ensembl GRCh38 transcriptome (release 106) using kb_python (RRID:SCR_018213) command kb count (v0.27.3) with kmer size = 31. Spliced and unspliced matrices were merged to create the count matrix for downstream analysis. The snRNA-seq analysis was performed according to best practices (29), using R Project for Statistical Computing (RRID:SCR_001905) (v4.4.1) and RStudio (RRID:SCR_000432) Server (v2024.09.0 build 375) with SingleCellExperiment (RRID:SCR_026794) (30) (v1.24.0) and Seurat (RRID:SCR_016341) (31) (v4.3.0.1) tools, and mamba (https://github.com/mamba-org/mamba) (v1.4.4) for version control. Poor quality cells were removed by filtering on a per-sample basis for low number of cells and features and high mitochondrial ratio. Ambient RNA was detected using the decontX function from celda (v1.14.0) (32), and droplets with decontX score > 0.3 were removed. Genes with >2% ambient contamination were removed (8 genes). Doublets were calculated and removed with scDblFinder (33) (v1.12.0). Ambient RNA was then detected again using SoupX (RRID:SCR_019193) (34) (v1.6.2) using parameters customized to each sample. Highly contaminated droplets (>30% soupX contamination) were removed and the soupX-adjusted count matrix was used for downstream analysis.

Data integration, clustering, and broad annotation.

Using Seurat, all datasets were merged, log-normalized, 5,000 variable features were selected, the data were scaled, and 50 PCs were calculated. A custom script was used to convert the Seurat object to Anndata (RRID:SCR_018209) format. Integration across patient and sequencing batch was performed using scvi-tools (RRID:SCR_026673) (35) (v1.0.2) using Jupyter Notebook (RRID:SCR_018315) (v7.2.1). Ray autotune was used to select optimal hyperparameters, which were then used in the scVI model. The model was trained using vae.train for 60 epochs, then latent representation embeddings were extracted and returned to the Seurat object for downstream visualization and analysis. Calculation of neighbors, Louvain clustering, and dimensionality reduction were then performed in Seurat using the scVI embeddings and 40 PCs. Integration success was measured using elbow plots, and calculation of LISI scores (LISI v1.0) (36). Clustree (RRID:SCR_016293) (v0.5.0) was used to assess optimal clustering resolution (37). Each cluster comprised cells from at least three patients and no one cluster had >80% cells from one patient, with the exception of B cells, which were mostly from patient MSK1687 (96.8%). Specific marker genes were calculated using Seurat FindAllMarkers() and visualized using Seurat DoHeatmap() and scDotPlot (v1.1.0). Broad cell-type annotations were assigned according to expression of canonical marker genes described in the literature visualized with Seurat DotPlot(). SCpubr (v2.0.2) was used for improved visualization (38).

Fine annotation.

Each broad cell type comprising fibroblasts, muscle cells (skeletal muscle cells and satellite cells), immune cells (macrophages, T cells, B cells, plasma cells, and granulocytes), and nonfibroblast stromal cells (adipocytes, lymphatic endothelial cells, vascular endothelial cells, Schwann cells, and mural cells) was then subset and reclustered using the methods described above. Crucially, this allowed feature selection (2,000 variable genes) and dimensionality reduction to be specific to each cell subset, revealing additional distinct cell types that were defined according to literature markers and/or highly expressed genes. Integration of the muscle subset with scVI failed quality control as several clusters contained >80% of cells from one patient so in this case reintegration was performed with Harmony (RRID:SCR_022206) (36) (v1.2.0). In some cases, smaller clusters were merged if they did not express biologically meaningful distinct marker genes.

Differential abundance of cell types across microanatomy.

MiloR (RRID:SCR_025630) (39) (v1.10.0) was used to assess differential abundance of broad cell types or fibroblasts across microanatomy using broad or fine annotations.

Downloaded from journals.physiology.org/journal/ajpcell (090.211.155.175) on May 11, 2026.

Differential gene expression and pathway enrichment.
To determine differential gene expression (DGE) within each broad cell type across microanatomy, gene expression was pseudobulked per cell type using Seurat AggregateExpression(), with genes with less than 10 reads filtered out. DESeq2 (RRID:SCR_015687) (40) (v1.40.2) was used to identify differentially expressed genes across microanatomy using the design formula "~ patient + microanatomical_site," and the likelihood ratio test (LRT) was used to compare multiple conditions. Pre- and post-QC heatmaps and PCA plots were generated, and comparisons were only drawn where cells from at least three donors were present at each microanatomy. Differentially expressed genes were clustered and visualized using DEGreport (RRID:SCR_018941) (v1.36.0). ClusterProfiler (RRID:SCR_016884) (41) (v4.10.0) was used to obtain enriched Gene Ontology: Biological Process (GO:BP) pathways on genes from groups of clusters into the following defined classes: enthesis-high, muscle-high, and tendon-high. A custom background of all genes expressed in that cell type was given and results were plotted using ggplot2 (RRID:SCR_014601). The same methods were also used to assess pathways enriched in each fibroblast subtype. Gene expression in each fibroblast subtype was aggregated by pseudobulk and the top 200 genes by number of counts was as the input to clusterProfiler.

Ligand-receptor interactions.
Liana (42) (v0.1.14) was used to identify ligand-receptor interactions between finely annotated cell types at each microanatomy, using CellPhoneDB (RRID:SCR_017054) and selecting interactions with a *P* value of at least 0.05. CrossTalkeR (43) (v1.4.0) was used to visualize overall ligand-receptor interactions using plot_cci(), and liana_dotplot was used to visualize specific interactions between selected cell types.

Spatial Transcriptomics

Sample preparation and 10X Xenium.
Representative tissue samples of the three tendon microanatomies and adjacent muscle were selected from one patient (MSK1687) based on initial hematoxylin and eosin (H&E) staining. Regions of interest (ROIs) were identified and embedded into a Tissue Array measuring 10.45 mm × 22.45 mm, corresponding to the dimensions of the Sample Area on 10X Genomics Xenium slides. Sectioning was performed as per Xenium "In Situ- Tissue Preparation Guide protocol" (10X Genomics, Demonstrated Protocol, CG000578 Rev E). Sections (5 µm) were cut and briefly placed in Milli-Q water at 37°C, then transferred to the Xenium slide (PN-3000941). Slides were kept upright at 40°C until excess water had dripped off and evaporated, then baked at 45°C for 3 h. The slides were stored in a desiccator at room temperature until they were ready for Xenium analysis. Slides underwent deparaffinization and decrosslinking according to the 10X Xenium "In Situ for FFPE-Deparaffinization and Decrosslinking Protocol" (10X Genomics, CG000580 Rev E) and using the Xenium Slides and Sample Prep Reagents Kit (10X Genomics). Hybridization was performed according to the Xenium In Situ Gene Expression User Guide (10X Genomics, CG000749 Rev B) C with a Probe Hybridization Mix containing a bespoke Add-On Custom Probe Panel (gene list in Data S3) of 101 genes designed to differentiate cell types found in the scRNA-seq data and the Xenium Human Multi Tissue and Cancer Probe Panel of 377 genes. Standard protocols were followed for cell segmentation staining, and analysis was performed using a Xenium Analyzer (RRID:SCR_023910) according to the Xenium Analyzer User Guide (10X Genomics, CG000584 Rev J). Following analysis, slides were stored at 4°C under PBS-Tween.

Post-Xenium H&E staining.
H&E staining was performed according to Xenium's Post-Xenium Analyzer H&E Staining (10X Genomics, CG000613 Rev A) protocol. Coverslips were mounted on the slides with DPX, and the slides were imaged with MoticEasyScan One digital slide scanner (RRID:SCR_024855).

Spatial Transcriptomics Data Analysis

Xenium data were processed using the 10X Genomics Xenium Onboard Analysis (RRID: SCR_026158). Output files were analyzed using Seurat (RRID:SCR_016341) v5.3.0 in R (RRID:SCR_001905) v4.5.1 with RStudio (RRID: SCR_000432) Server Pro build 467.pro1. Filtering was performed according to cell size, number of transcripts, and number of probes. Data from all four tissue pieces were integrated using Harmony (RRID:SCR_022206) with Seurat IntegrateLayers(). Normalization was performed using SCTransform (RRID:SCR_022146), and the Seurat workflow was followed for dimensionality reduction [RunPCA(), RunUMAP()]. Annotation was performed by transferring broad and fine annotation labels from the snRNA-seq data using FindTransferAnchors() and TransferData(). Broad cell types (immune, fibroblast, muscle, and stromal) were subsetted, and the above steps were repeated to define the finely annotated cell types. Annotations were uploaded to 10x Genomics Xenium Explorer (RRID:SCR_025847) along with post-Xenium H&E staining to generate figures. SCpubr_2.0.2 was used for Uniform Manifold Approximation and Projection (UMAP) plots.

RESULTS

Cellular Composition of the Achilles Tendon Reflects Its Microanatomical Structure

To study the tissue morphology and cell types present in the Achilles tendon, we collected tissue from microanatomical sites: tendon proximal to the enthesis, tendon midbody, tendon proximal to the MTJ, and adjoining muscle (Fig. 1*A*). We used histological staining to compare tissue features across microanatomy (Supplemental Fig. S1). Across the whole tendon, densely packed fascicular tendon was visible, interspersed with interfascicular matrix. Surrounding this was peritendon rich in blood vessels, nerves, and adipocytes. At the enthesis, the junction between tendon fibrils and minimally cellular fibrocartilage was clearly visible. The muscle-tendon interaction was apparent at the MTJ, although muscle fibers extended into the tendon midbody. The muscle tissue section showed skeletal muscle fibers alongside a stromal section encompassing vessels and nerves, much like the peritendon.

Downloaded from journals.physiology.org/journal/ajpcell (090.211.155.175) on May 11, 2026.

We isolated nuclei from tissue across the Achilles tendon from five patients (Fig. 1*A* and Table 1) and performed single-nucleus RNA sequencing (snRNA-seq). After quality control and integration (Supplemental Fig. S2), we obtained 64,862 nuclei and assigned each to its putative cell type of origin. Using canonical markers, we found 13 broad cell types including fibroblasts (*DCN*, *COL1A2*), skeletal muscle cells (*TTN*, *NEB*) and their precursor satellite cells (*PAX7*, *CALCR*), immune cells comprising macrophages (*CD163*, *MRC1*), T cells (*THEMIS*, *CD247*), granulocytes (*KIT*, *IL18R1*), B cells (*BLNK*, *FCRL1*), and plasma cells (*JCHAIN*, *XBP1*), and nonfibroblast stromal cells comprising vascular endothelial cells (VEC; *PECAM1*, *VWF*), lymphatic endothelial cells (LEC; *PROX1*, *PKHD1L1*), mural cells (*NOTCH3*, *MYO1B*), and adipocytes (*ADIPOQ*, *AQP7*; Fig. 1*B* and Supplemental Fig. S3). We sought to determine the variation in cell-type abundance across the tendon using quantitative differential abundance testing (Fig. 1*C*) and analysis of cell proportions (Fig. 1*D* and Supplemental Fig. S4). Spatial transcriptomics by 10X Xenium with postanalysis H&E staining was performed to facilitate visualization of the cell positioning within the densely fibrous tendon tissue and muscle (Fig. 1, *E* and *F*). Fibroblasts were the most numerous cell type (37% of nuclei) and were present throughout the length of the tendon from the junction with fibrocartilage to the MTJ and in muscle. Spatial transcriptomics confirmed that fibroblasts (red) were located in the peritendon and fascicular tendon, as well as adjacent to muscle fibers (Fig. 1*F*). From the differential abundance testing, it appeared that fibroblasts had a wide spread of neighborhood enrichment, suggesting that there might be fibroblast subsets specific to each microanatomical zone (Fig. 1*C*). Unsurprisingly, skeletal muscle cells and satellite cells were highly enriched at the muscle and MTJ and were almost absent from the enthesis-proximal tendon (Fig. 1*C*), and in spatial data, the myonuclei could be seen surrounding muscle fibers (Fig. 1*F*). The peritendon structure and cellular composition seemed consistent across microanatomy and contained adipocytes (yellow), mural cells (green) and VEC (pink) cells visible around blood vessels, Schwann cells (dark blue) in peripheral nerve bundles, and small numbers of immune cells (mostly macrophages, light blue) (Fig. 1, *E* and *F*). The muscle samples also contained cells associated with blood vessels, nerves, and lymphatic structures. Small populations of T cells, B cells, plasma cells, and granulocytes were identified in the snRNA-seq data but were rarely detected spatially. Overall, these findings confirmed the cellular composition and spatial position of broad cell types and led us to consider whether smaller cell subtypes, particularly fibroblasts, might have specialist locations across the Achilles tendon.

Distinct Fibroblast Subsets with Unique Functional Properties Are Found across the Achilles Tendon

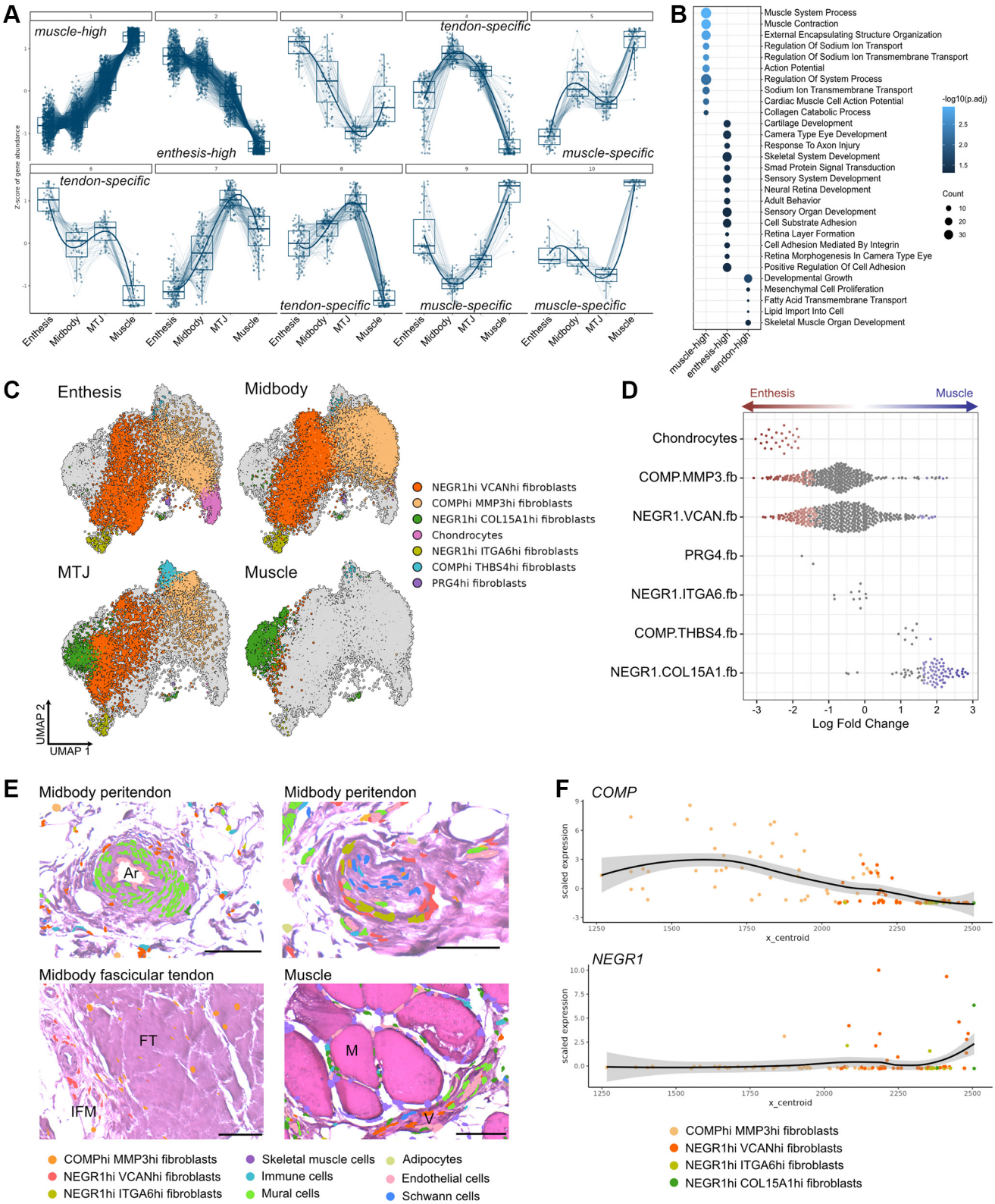
Next, we identified which genes were differentially expressed (DE) across the Achilles tendon microanatomy within each broad cell type. Although most cell types had relatively few DE genes (<1,000), fibroblasts had over 5,000 DE genes (Supplemental Fig. S5*A*). By clustering the genes according to their expression profiles across microanatomy, we found 10 distinct groups of DE genes from fibroblasts (Fig. 2*A*). The two largest clusters were those with the highest expression in the muscle (cluster 1; 761 genes) or at the enthesis (cluster 2; 491 genes). We also identified tendon-specific gene clusters with high expression across tendon and low expression in muscle (clusters 4, 6, and 8; 245 genes), and muscle-specific gene clusters with high expression in muscle and low expression in tendon (clusters 5, 9, and 10; 133 genes). Pathway analysis on these combined gene clusters revealed enrichment of distinct biological pathways for each gene expression pattern, such as muscle-related pathways for gene clusters with high expression in muscle, and adhesion-related pathways for clusters with high expression in enthesis (Fig. 2*B*). These findings led us to consider whether annotation at finer resolution could identify fibroblasts with more specialist locations and functions.

We performed fine-resolution annotation of fibroblasts in the snRNA-seq data by testing cell-type clustering at several resolutions. We compared outputs from Clustree, heatmaps of marker gene expression, and expression pattern of canonical marker genes to determine which biologically relevant resolution to use for detailed annotation. At the chosen resolution, we identified six fibroblast subtypes and chondrocytes (Fig. 2*C* and Supplemental Fig. S5, *B*–*H*). The five biggest clusters could be broadly classed into two groups, expressing *NEGR1* and *COMP*, and more specifically using additional markers *VCAN*, *MMP3*, *COL15A1, ITGA6*, and *THBS4*. In addition, two smaller clusters were found and identified as chondrocytes (*ACAN*) and PRG4hi fibroblasts (*PRG4*). Each subtype expressed genes enriched in specific biological pathways (Supplemental Fig. S5*I*). Differential abundance analysis of the fibroblast subsets which, along with variation in relative proportion of nuclei, suggested striking differences in the distribution of fibroblast subtypes across microanatomy (Fig. 2, *C* and *D* and Supplemental Fig. S5, *J*–*L*). Expression of highly DE genes across microanatomy seemed to correlate with genes that are highly expressed in fibroblast subtypes that are mostly present in that microanatomy (Supplemental Fig. S5*M*), suggesting that the variation is due to alterations in cell composition rather than transcriptional changes across microanatomy within a particular fibroblast.

To uncover the spatial location and organization of these specialist fibroblasts within the tendon and muscle tissue, we used spatial transcriptomics (Fig. 2*E*). The most abundant fibroblast populations were NEGR1hi VCANhi fibroblasts (44% of nuclei) and COMPhi MMP3hi fibroblasts (40% of nuclei), which were both present in all tendon microanatomies but absent from muscle. NEGR1hi VCANhi fibroblasts were present in the peritendon and interfascicular matrix adjacent to blood vessels and nerves, while COMPhi MMP3hi fibroblasts were found in the fascicular tendon (Fig. 2*E*). Consistent with this, COMPhi MMP3hi fibroblasts expressed genes in pathways related to extracellular matrix adhesion (Supplemental Fig. S5*H*). Expression of the key marker genes *COMP* and *NEGR1* correlated spatially with the location of COMPhi MMP3hi and NEGR1hi VCANhi fibroblasts across a cross-section of the field of view in midbody and confirmed that these two populations have nonoverlapping spatial locations in the tendon tissue (Fig. 2*F*). NEGR1hi ITGA6hi fibroblasts were found surrounding peripheral nerves in the tendon and muscle, so appear to be perineural fibroblasts (Fig. 2*E*). NEGR1hi COL15A1hi fibroblasts were positioned

Downloaded from journals.physiology.org/journal/ajpcell (090.211.155.175) on May 11, 2026.

surrounding the muscle fibers in the muscle tissue section (Fig. 2*E*). The small number of COMPhi THBS4hi fibroblasts were predominant at the MTJ in snRNA-seq, but not detected in the spatial data (Fig. 2, *C* and *D*, and Supplemental Fig. S5*J*). Finally, chondrocytes (*ACAN-expressing* cartilage matrix-producing cells) and PRG4hi fibroblasts were detected in the snRNA-seq data but not in the spatial data, with chondrocytes specific to the enthesis and PRG4hi fibroblasts



AJP-Cell Physiol • doi:10.1152/ajpcell.00838.2025

Downloaded from journals.physiology.org/journal/ajpcell (090.211.155.175) on May 11, 2026.

present in the tendon but not muscle (Fig. 2, *C* and *D*, and Supplemental Fig. S5, *K* and *L*).

We performed SCENIC analysis (44) and identified transcriptional networks (regulons) specifically enriched in each fibroblast subset, providing further evidence of their functional specialization (Supplemental Fig. S5*N*). For example, the IRF3 regulon, known to regulate collagen production in fibrosis (45), was enriched in COMPhi MMP3hi fibroblasts, whereas the MYF6 regulon was enriched in MTJ/muscle-resident COMPhi THBS4hi and NEGR1hi COL15A1hi fibroblasts, perhaps conferring contractile properties in these cells (46).

Fine Annotation of Nonfibroblast Cell Types

Fine annotation of the nonfibroblast cell types—muscle cells, immune cells, and nonfibroblast stromal cells—revealed 22 distinct subtypes in snRNA-seq data (Fig. 3 and Supplemental Fig. S6–S8). Within the nonfibroblast stromal cells, the adipocytes, LEC, and Schwann cells did not display any further subsets, but arteriolar (*PODXL, EFNB2,* and *NEBL*) and venular VEC (*NOSTRIN, MYRIP,* and *GNA14*) were distinguishable as well as pericytes (*PDGFRB, EGFLAM,* and *RIMS1*) and vascular smooth muscle cells (vSMCs; *MYH11, RCAN2,* and *LMOD1*) (Fig. 3*A* and Supplemental Fig. S6). Differential abundance analysis suggested moderate changes in the distribution of cell neighborhoods across the Achilles tendon, especially pericytes which were highly enriched toward muscle (Fig. 3*A*). All stromal cells were observed in H&E-defined cross-sections of veins, arteries, nerves, lymphatic structures, and adipose in tendon and muscle using spatial transcriptomics (Fig. 3, *D*–*G*).

Macrophages were the most abundant immune cells in snRNA-seq data, comprising a major population of tissue-resident MERTKhi LYVEhi macrophages alongside MERTKhi LYVE1lo and MERTKlo PTPRGhi macrophage populations (47). Fine annotation also revealed monocytes, CLEC10Ahi and CLEC9Ahi dendritic cells (DCs) and NK cells, alongside T cells, B cells, plasma cells, and granulocytes (Fig. 3*B* and Supplemental Fig. S7). Although some differential abundance analysis suggests MERTKlo PTPRGhi macrophages were enriched toward the enthesis and some small neighborhoods of granulocytes, T cells, and MERTKhi LYVE1hi macrophages were enriched toward the muscle, most immune cell types did not show striking changes across microanatomies in snRNA-seq data (Fig. 3*B*). The major immune cell groups (DC, monocytes, granulocytes, T cells, and macrophages) were detectable in the spatial transcriptomics data, in or adjacent to blood vessels in both tendon and muscle (Fig. 3, *D*–*G*).

The muscle cell populations predominantly comprised classical slow-twitch (type I) and fast-twitch (type II) myocytes. Transitional myocytes were annotated by expression of both slow- and fast-twitch markers as well as *COL22A1*, an MTJ marker (48), and satellite cells (myocyte precursors) were identified using *PAX9* (Fig. 3*C* and Supplemental Fig. S8). Differential abundance analysis revealed that neighborhoods of each subset were enriched toward the MTJ and muscle (Fig. 3*C*). Slow- and fast-twitch muscle nuclei were observed spatially surrounding distinct muscle fibers (Fig. 3*G*), and small numbers of transitional muscle cells and satellite cells could also be seen in the muscle section. A bundle of slow-twitch muscle fibers was seen in the tendon midbody section, indicating that the muscle fibers can extend deeply into the tendon structure (Supplemental Fig. S8*E*). Unexpectedly, unlike in the histological staining, we did not detect any muscle cell types in the MTJ spatial transcriptomics section, which is likely a sampling issue.

Cell-Cell Interactions Are Dependent on Cell Composition and Fibroblast Function

Having identified differences in spatial positioning of fibroblasts across tendon microanatomy, we next identified predicted cell-cell interactions between all the cell types found in the Achilles tendon (Fig. 4*A*). Overall, there were more ligand-receptor interactions in muscle than in tendon, and fibroblasts were the cell type with the most interactions. The number of interactions appeared to relate to cell composition, with more abundant cells having more interactions at a particular microanatomy. For example, chondrocytes showed strong interactions with NEGR1hi VCANhi fibroblasts only in the enthesis, whereas NEGR1hi COL15A1hi had more interactions with COMPhi THBS4hi fibroblasts in MTJ and muscle. We therefore focused on interactions between specific fibroblast subtypes and nonfibroblast cells (Fig. 4, *B*–*D*). Very few interactions were seen between fibroblasts and immune cells or muscle cells in tendon tissue (Supplemental Fig. S9). NEGR1hi COL15A1hi fibroblasts (resident in muscle) and NEGR1hi VCANhi fibroblasts (in vessel-rich peritendon) express *SCARA5* (scavenger receptor 5 class A), which is predicted to interact with *VWF* (Von-Willebrand Factor) on vascular endothelial cells (Fig. 4*B*). In addition, the NEGR1hi COL15A1hi fibroblasts express several ECM genes (*MMP2*, *COL4A1*, *COL4A2*) which are predicted to bind receptors on the vascular endothelial cells (*PECAM1*, *CD93*) (Fig. 4*C*). NEGR1hi ITGA6hi fibroblasts, found in nerve bundles, showed specific interaction with Schwann cells in the nerve

Figure 2. Phenotypic and functional characterization of fibroblast subtypes. *A*: scaled gene expression in fibroblasts clustered by expression patterns across tendon microanatomy ($n = 5$). Groups of genes with particular cluster profiles are indicated (muscle-high, enthesis-high, tendon-specific, and muscle-specific). *B*: dotplot showing GO:BP pathways enriched in clusters with muscle-high expression, enthesis-high expression, or tendon-high expression. Although 133 muscle-specific genes were found, these were not enriched in any pathways. *C*: UMAP representation of the fibroblast subset showing fine cell-type annotations split by microanatomy. *D*: beeswarm plot showing differential abundance of each fibroblast subtype across microanatomy, calculated using MiloR. Each dot represents one cellular neighborhood comprising tens to hundreds of similar cells; red and blue color indicates neighborhoods with significantly greater abundance at the enthesis or muscle, respectively. *E*: spatial transcriptomics plots showing fibroblast subtypes overlaid onto post-Xenium H&E images ($n = 1$). *Top, left*: NEGR1hi VCANhi fibroblasts positioned near an artery (A)v in peritendon from tendon midbody. *Bottom, left*: COMPhi MMP3hi fibroblasts in the fascicular tendon (FT) and NEGR1hi VCANhi fibroblasts in the interfascicular matrix (IFM) from midbody. *Top, right*: NEGR1hi ITGA6hi fibroblasts surrounding a peripheral nerve bundle (PNB) in peritendon from tendon midbody. *Bottom, right*: NEGR1hi COL15A1hi fibroblasts interspersed with muscle fibers (M) and vessels (V) in muscle. Scale bar: 100 μm. *F*: dotplot showing scaled expression of *COMP* and *NEGR1* according to fibroblast subtype along a cross section of tendon midbody (x-centroid). Black line shows smoothed expression calculated by ggplot2 geom_smooth() with standard error in gray.

Downloaded from journals.physiology.org/journal/ajpcell (090.211.155.175) on May 11, 2026.

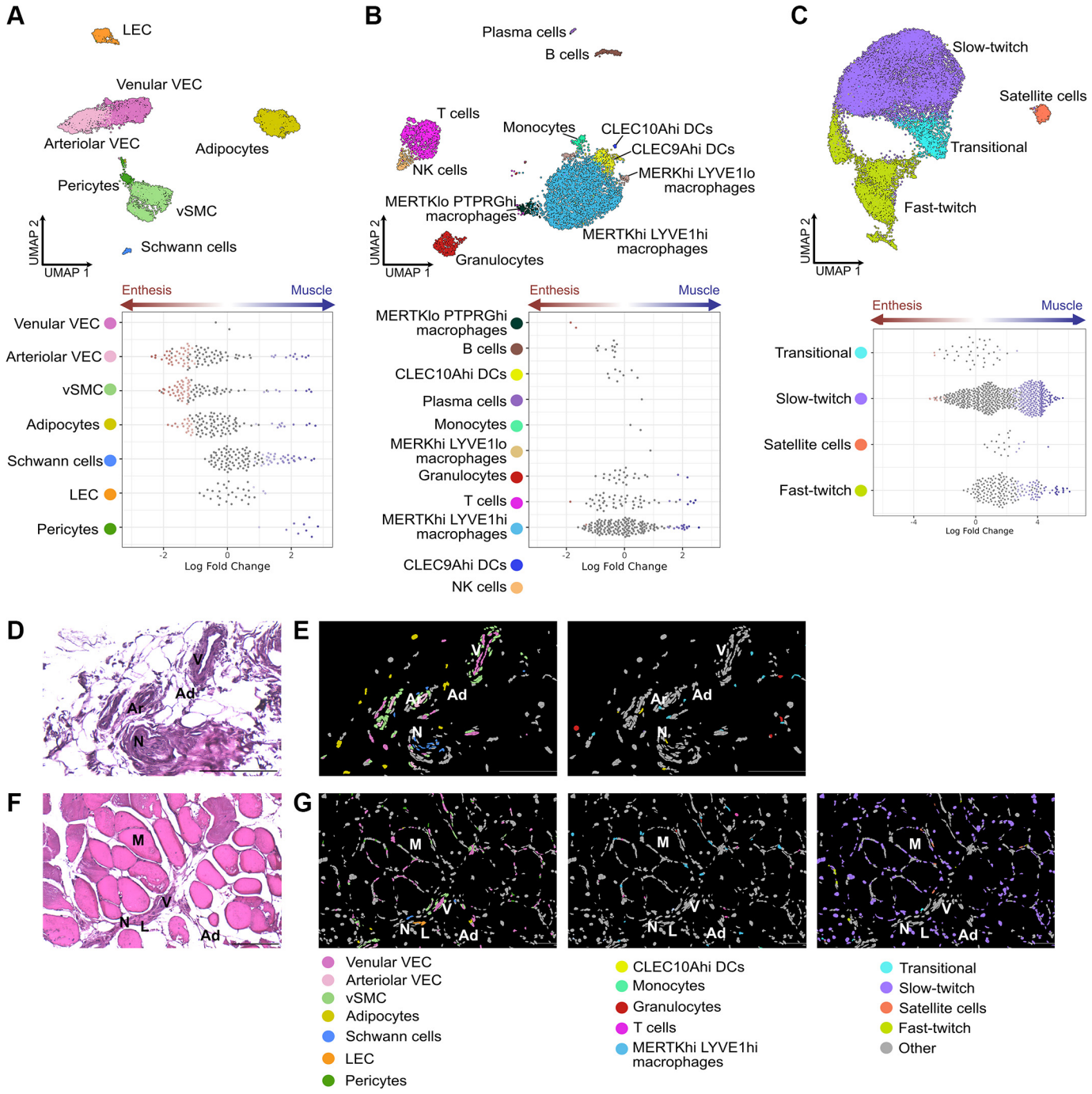


Figure 3. Fine annotation of nonfibroblast cell types identified in Achilles tendon ($n = 5$). *A–C*: UMAP representations (*top*) and Beeswarm plots (*bottom*) from stromal subset, immune subset, and muscle subset. UMAP representations are colored by fine annotation level; Beeswarm plots show differential abundance of each finely annotated cell type across microanatomy calculated using MiloR. Immune cell subtypes CLEC9Ahi DCs and NK cells did not form distinct neighborhoods as they were few in number. *D–G*: H&E staining and spatial transcriptomics images showing tissue position of finely annotated cell types. *D*: H&E image from Achilles tendon midbody, showing blood vessels, adipocytes, and a peripheral nerve bundle in the peritendon ($n = 1$). *E*: spatial transcriptomics plots of the same field of view as *D* colored by stromal (*left*) or immune (*right*) cell types ($n = 1$). *F*: H&E image from muscle, showing muscle fibers, veins, nerves, and lymphatic vessels. *G*: spatial transcriptomics of the same field of view as *F* colored by stromal (*left*), immune (*middle*), or muscle (*right*) cell types. Other cell types are colored gray, and scale bars are 200 μm. Ad, adipose; Ar, artery; L, lymphatic vessel; M, muscle; N, nerve bundle; V, vein.

via *NRXN1* (Neurexin-1) – *NLGN1* (Neuroligin-1) (Fig. 4*D*). This analysis reveals that the interactions between fibroblasts and other cells are influenced by their spatial position in these tissues, providing additional insights into their putative functions.

DISCUSSION

This study presents the first cellular atlas of the human Achilles tendon and associated muscle in which macroscopic differences in tissue architecture were mirrored at

Downloaded from journals.physiology.org/journal/ajpcell (090.211.155.175) on May 11, 2026.

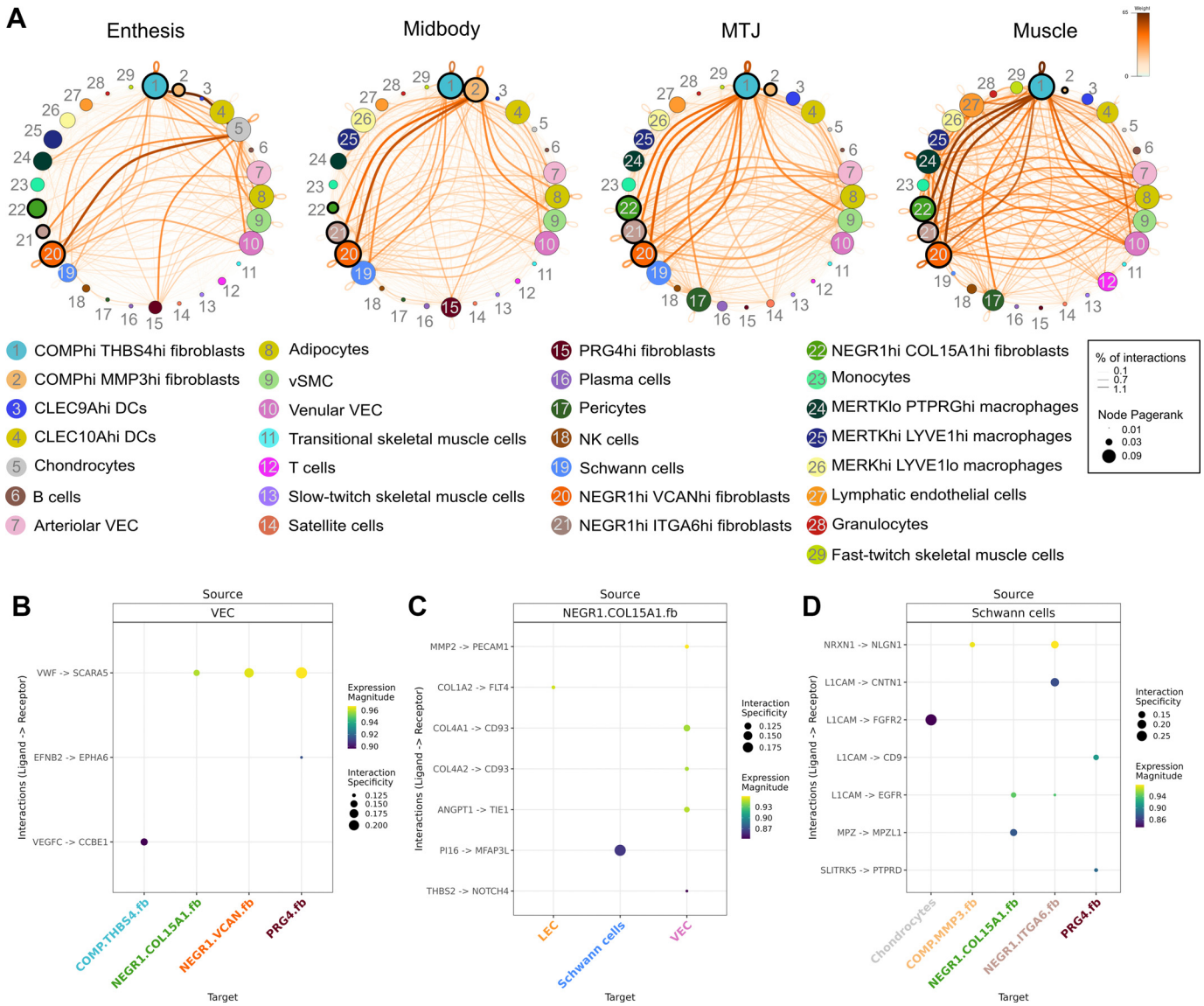


Figure 4. Predicted cell-cell interactions across cell types in Achilles tendon. *A*: cell-cell interaction plots showing ligand-receptor interactions at each microanatomy calculated using LIANA. Each node on the circumference represents a cell type (demarked with a bold black line for fibroblasts), with the size of the dot related to the number of interactions with that cell type (Pagerank). Interactions are depicted by lines between the dots, with the thickness representing the percent of total interactions and color representing the weight of the interaction. Dotplot shows specific ligand-receptor interactions between VEC and fibroblasts (*B*), NEGR1hi COL15A1hi fibroblasts and stromal cells (*C*), and Schwann cells and fibroblasts (*D*). COMP.MMP3.fb, COMPhi MMP3hi fibroblasts; COMP.THBS4.fb, COMPhi THBS4hi fibroblasts; NEGR1.COL15A1.fb, NEGR1hi COL15A1 fibroblasts; NEGR1.ITGA6.fb, NEGR1hi ITGA6hi fibroblasts; NEGR1.VCAN.fib, NEGR1hi VCANhi fibroblasts.

the cellular level, reflecting the functional properties of each microanatomical zone. Notably, six distinct fibroblast subtypes were defined, each with specific transcriptional profiles, alongside stromal, immune, and muscle cell phenotypes, consistent with those reported in other tendon studies (15–25). By including high-resolution spatial transcriptomic data, we have been able to identify the exact locations of most fibroblast subsets within the tendon and muscle tissue relative to the tendon matrix, vessels, nerves, muscle fibers, and nonfibroblast cell types. Transcriptional variation along the length of the tendon was due to changes in cellular composition rather than expression changes within cell types. Some fibroblast subsets are enriched within a particular microanatomical zone and have unique cell-cell interactions. Taken together, we were able to predict functions of each fibroblast subtype that contribute to the microanatomical niches across the tendon and associated muscle, which broadly align with those described in the literature.

At the expression level, five of the fibroblast subsets we identified within the Achilles tendon fell into two broad groups defined by the expression of *COMP* and *NEGR1* (Supplemental Fig. S5, *F* and *G*); these two subsets have similar gene expression profiles to the MKX$^+$ (*COMP*, *ITGA10*, *THBS4*, *COL12A1*) and PDGFRA$^+$ (*NEGR1*, *FBN1*, *DCLK1*) fibroblasts found in hamstring tendon, respectively (16). COMPhi MMP3hi fibroblasts (40% of fibroblasts) and NEGR1hi VCANhi fibroblasts (44% of fibroblasts) were

Downloaded from journals.physiology.org/journal/ajpcell (090.211.155.175) on May 11, 2026.

present across all tendon microanatomies but absent from the muscle, so are likely to be "tenocytes" or tendon-specific fibroblasts. COMPhi MMP3hi fibroblasts were located in the fascicular tendon, expressed genes related to matrix adhesion (Fig. 2), and were enriched for regulons *FLI1* and *IRF3* (Supplemental Fig. S5), which are known to regulate collagen production (45, 49). As such, these fibroblasts appear to be required for maintenance of the ECM that comprises the fascicular tendon and are similar to FBLN1hi fibroblasts (*COMP*, *FBLN1*, *CILP*) in healthy quadriceps tendon (15, 25) and fibroblast subset Fib2 (*COMP, ITGA10*) in hamstring tendon (24). NEGR1hi VCANhi fibroblasts expressed genes related to cell morphogenesis consistent with their position surrounding blood vessels and nerves in the peritendon and interfascicular matrix (Fig. 2), with comparable expression phenotype and location to the Fib3 fibroblast subset (*NEGR1, PDGRA, VCAN*) in hamstring tendon (24). Cell-cell communication analysis indicated a direct interaction between NEGR1hi VCANhi fibroblasts and vascular endothelial cells via *SCARA5-VWR*, so they likely have a structural role supporting tendon vascularization and innervation. Fibroblast-enabled neovascularization is a hallmark of Achilles tendinopathy (50), so the role of NEGR1hi VCANhi fibroblasts in disease pathogenesis remains an important topic for future study.

NEGR1hi ITGA6hi fibroblasts were observed across the whole tendon and associated muscle and were spatially located surrounding peripheral nerve bundles. They expressed genes related to cell junctions and neurons/axons and interacted directly with Schwann cells via *NRXN1-NLGN1*. The same interaction was observed in a snRNA-seq study of human NF1-associated plexiform neurofibroma, a tumor arising from Schwann cells (51), but the functional relevance of this interaction in tendon remains to be elucidated. NEGR1hi ITGA6hi fibroblasts had similar gene expression patterns to the hamstring tendon "nerve cells" (*TENM2, SLC22A3*) (16), quadriceps tendon ABCA10+ fibroblasts (*ACBA10, CNTN4*) (15, 25), Fib4 perineural fibroblasts (*ITGA6*) (24), and also to endo- and perineurial fibroblasts found in skeletal muscle (*ITGA6, SLC22A3*) (52), so are likely nerve-associated or perineural fibroblasts. As injuries to the Achilles tendon are a significant health issue (53, 54), the role of these cells should be of special interest in future studies in terms of prevention and modulation of pain in tendon pathologies.

COMPhi THBS4hi fibroblasts and NEGR1hi COL15A1hi fibroblasts were mainly detected in MTJ, or in muscle and MTJ, respectively. Both these fibroblast subsets were enriched for muscle-related processes and the *MYF6* regulon, a myogenic transcription factor, suggesting that these fibroblast types support the formation of muscle fibers. NEGR1hi COL15A1hi fibroblasts had a similar transcriptional profile to parenchymal fibroblasts in muscle (*COL15A1, COL4A1, ALDH1A2*) (52) as well as "universal" fibroblasts found across multiple tissues (*COL15A1, COL4A1, HSPG2*) (55, 56), indicating that they are likely a common fibroblast present in muscle and other nontendon tissues. As *THBS4* was abundant in fibroblasts from mouse Achilles MTJ (26) and two studies from hamstring MTJ (20, 24), the COMPhi THBS4hi fibroblasts identified in our snRNA-seq data are likely an MTJ-specific subset.

A small number of *PRG4hi* fibroblasts were detected in the snRNA-seq data, predominantly in the tendon enthesis and midbody zones. The key marker *PRG4* (lubricin) facilitates biological lubrication, for example, as part of the synovial fluid. Although mainly known as a key marker for lining layer fibroblasts in synovium (57, 58), expression of *PRG4* has previously been shown in fibrocartilaginous region of tendon and has been proposed to be important for surface lubrication of the tendon sheath (59).

Chondrocytes were defined by their expression of canonical markers (*ACAN, COL2A1, WWP2*) and enrichment of the SOX9 regulon, a known regulator of chondrocytes. These cells show similarity to the chondrocytes found in supraspinatus tendon (22) and prehypertrophic chondrocytes in cartilage (60). The presence of these cells specifically in tendon enthesis zone single-nuclei data is in accordance with the presence of collagen II and aggrecan in enthesis, but not midbody of tendon (61).

Over 20 (sub)types of nonfibroblast cells were identified. Apart from skeletal muscle cell types that were highly enriched in the MTJ and muscle regions, few cell types showed strong regional changes, like those found with fibroblast subsets. This supports the hypothesis that tendon fibroblasts are not only critical for the construction and maintenance of tendons as key producers of ECM but also support the establishment of specialized tissue niches through cell-cell interaction of varying fibroblast subsets with other resident cell types. The existence of the proposed specialized fibroblast subsets in health raises the question of how these different subsets are affected by different pathologies. The Achilles is the most heavily mechanically loaded tendon in the human body and the most frequently injured, with consequent burden on society and healthcare systems. Previous studies have shown that genetic variants at the *MMP3* locus, a gene highly expressed in the COMPhi MMP3hi fibroblasts, are associated with Achilles tendinopathy (62), implicating this specific fibroblast subset with the disease. Future elucidation of the cellular basis of pathogenesis of Achilles tendinopathies, including assessment of microanatomical differences in disease susceptibility, will lead to long-term improvements in patient care.

Healthy tendon tissue is challenging to acquire for research, making this dataset a valuable resource. In this study, we obtained tendon tissue from patients undergoing an amputation due to sarcoma but with no active or previous tendon disease. The Achilles tendons all looked macroscopically and microscopically normal with no identified tears, came from older adult donors (age 45–76), and donors were ambulant at the time of surgery. Identification of changes in cellular composition and transcriptional profile over human lifespan will be an important topic for future study.

Spatial transcriptomics was able to confirm the presence and location of most cell types, thereby adding a wealth of knowledge on specialized cell types and functions across microanatomy. However, the location of a few small (sub-) populations of cells could not be confirmed due to limitations of available tissue sections ($n = 1$), as well as a limited number of gene probes (480) used. For example, chondrocytes have been hypothesized to be present in small numbers, only forming 3–4 rows of cells at the bone-tendon interface (12), so while they were detected in snRNA-seq data

Downloaded from journals.physiology.org/journal/ajpcell (090.211.155.175) on May 11, 2026.

from the tendon enthesis zone, we were unable to confirm their location in the spatial data. Similarly, muscle fibers and corresponding associated fibroblasts were not captured in the MTJ spatial section. Future studies on a greater number of individuals and using complementary methods, such as immunofluorescence or immunohistochemistry, will be needed to confirm the findings presented here.

In conclusion, this transcriptomic atlas of human Achilles tendon describes the cellular composition of the tendon at unprecedented resolution, which has been vital to progress our understanding of the transitional nature of the bone-tendon-muscle unit. The changes in the presence and proportion of cell types, especially fibroblast subsets, across the different microanatomical zones of the Achilles tendon suggest functional niches that might be uniquely disrupted by injuries or autoimmune diseases. Therefore, this work forms a critical reference dataset for future studies on both tendon development and repair, and the pathologies affecting the different regions of the Achilles tendon and associated tissues.

DATA AVAILABILITY

Analysis code is available at https://github.com/Botnar-MSK-Atlas/achilles_tendon_atlas. Processed snRNA-seq is available via the CZI cellxgene database https://cellxgene.cziscience.com/collections/a7e81820-297d-4086-8123-cc7dde64e495. Raw snRNA-seq data files (fastq) will be available on request from the HCA Data Portal https://explore.data.humancellatlas.org/projects/893c8fb6-bf65-4527-b83b-8233de59244c.

SUPPLEMENTAL MATERIAL

Supplemental Figs. S1–S9: https://doi.org/10.6084/m9.figshare.31241065.

Supplemental Data S1–S5: https://doi.org/10.17632/vfzd93y7dv.1.

ACKNOWLEDGMENTS

We thank our research assistant Louise Appleton, our research nurses Debra Beazley and Lois Vesty-Edwards, and the surgical teams at the Nuffield Orthopaedic Centre for their invaluable help in collecting human tissue for this study. We acknowledge support from the Oxford Musculoskeletal Biobank and thank the patients for donating their tissue to research. We thank Joanna Hester and Audrey Au Young for assistance in running the Xenium experiments. Finally, we thank all other members of the CZI Tendon Seed Network for insightful discussions. Graphical abstract created with a licensed version of BioRender.com.

Preprint is available at https://doi.org/10.1101/2025.10.17.683019.

GRANTS

This work was funded by the following grants: Chan Zuckerberg Initiative Tendon Seed Network grant (Grant Nos.: 2019–002426, 2021–240342 to A.P.C., M.J.B., and S.J.B.S.), Arthritis UK (Grant Number: 22873 to J.Y.M.), Rhodes Scholarship (to T.B.S.), Oxford-Medical Research Council Doctoral Training Partnership (to A.K.), NIHR | NIHR Oxford Biomedical Research Centre (OxBRC), Medical Research Council (Grant No.: MR/V010182/1 to A.P.C.), and Paget's Association (Grant No.: PA21010 to P.A.H.).

DISCLOSURES

A.P.C. is a cofounder and employee of Caeruleus Genomics Ltd and is an inventor on several patents related to sequencing technologies filed by Oxford University Innovations. None of the other authors has any conflicts of interest, financial or otherwise, to disclose.

AUTHOR CONTRIBUTIONS

A.P.C., M.J.B., and S.J.B.S. conceived and designed research; J.Y.M., C.P., S.S., L.R-M., C.T.I., A.C.A., T.B.S., M.N., C.G., D.W., T.C., S.G., A.S., R.B.R., and H.B-W. performed experiments; C.J.C., J.Y.M., A.K., and K.R-A. analyzed data; C.J.C., J.Y.M., A.K., P.A.H., D.S., M.J.B., and S.J.B.S. interpreted results of experiments; C.J.C. prepared figures; C.J.C. drafted manuscript; C.J.C., J.Y.M., A.P.C., P.A.H., D.S., M.J.B., and S.J.B.S. edited and revised manuscript; C.J.C., J.Y.M., A.K., C.P., S.S., L.R-M., C.T.I., A.C.A., T.B.S., M.N., K.R-A., C.G., D.W., T.C., S.G., A.S., R.B.R., H.B-W., A.P.C., P.A.H., D.S., M.J.B., and S.J.B.S. approved final version of manuscript.

REFERENCES

1. **Doral MN**, **Alam M**, **Bozkurt M**, **Turhan E**, **Atay OA**, **Dönmez G**, **Maffulli N.** Functional anatomy of the Achilles tendon. *Knee Surg Sports Traumatol Arthrosc* 18: 638–643, 2010. doi:10.1007/s00167-010-1083-7.
2. **Hefferan SA**, **Blaker CL**, **Ashton DM**, **Little CB**, **Clarke EC.** Structural variations of tendons: a systematic search and narrative review of histological differences between tendons, tendon regions, sex, and age. *J Orthop Res* 43: 994–1011, 2025. doi:10.1002/jor.26060.
3. **Ackermann PW**, **Phisitkul P**, **Pearce CJ.** Achilles tendinopathy – pathophysiology: state of the art. *Journal of ISAKOS* 3: 304–314, 2018. doi:10.1136/jisakos-2017-000164.
4. **Traweger A**, **Scott A**, **Kjaer M**, **Wezenbeek E**, **Scattone Silva R**, **Kennedy JG**, **Butler JJ**, **Gomez-Florit M**, **Gomes ME**, **Snedeker JG**, **Dakin SG**, **Wildemann B.** Achilles tendinopathy. *Nat Rev Dis Primers* 11: 20, 2025. doi:10.1038/s41572-025-00602-9.
5. **Carmont MR**, **Gunnarsson B**, **Brorsson A**, **Nilsson-Helander K.** Musculotendinous ruptures of the achilles tendon had greater heel-rise height index compared with mid-substance rupture with non-operative management: a retrospective cohort study. *J ISAKOS* 9: 148–152, 2024. doi:10.1016/j.jisako.2023.12.006.
6. **Alvarez A**, **Tiu TK.** *Enthesopathies*. StatPearls Publishing, 2025.
7. **Baldwin M**, **Buckley CD**, **Guilak F**, **Hulley P**, **Cribbs AP**, **Snelling S.** A roadmap for delivering a human musculoskeletal cell atlas. *Nat Rev Rheumatol* 19: 738–752, 2023. doi:10.1038/s41584-023-01031-2.
8. **Winnicki K**, **Ochała-Kłos A**, **Rutowicz B**, **Pękala PA**, **Tomaszewski KA.** Functional anatomy, histology and biomechanics of the human Achilles tendon — A comprehensive review. *Ann Anat* 229: 151461, 2020. doi:10.1016/j.aanat.2020.151461.
9. **Tresoldi I**, **Oliva F**, **Benvenuto M**, **Fantini M**, **Masuelli L**, **Bei R**, **Modesti A.** Tendon's ultrastructure. *Muscles Ligaments Tendons J* 3: 2–6, 2013. doi:10.11138/mltj/2013.3.1.002.
10. **Jakobsen JR**, **Krogsgaard MR.** The myotendinous junction—a vulnerable companion in sports. A narrative review. *Front Physiol* 12: 635561, 2021. doi:10.3389/fphys.2021.635561.
11. **Knudsen AB**, **Larsen M**, **Mackey AL**, **Hjort M**, **Hansen KK**, **Qvortrup K**, **Kjær M**, **Krogsgaard MR.** The human myotendinous junction: an ultrastructural and 3D analysis study. *Scand J Med Sci Sports* 25: e116–e23, 2015. doi:10.1111/sms.12221.
12. **Apostolakos J**, **Durant TJ**, **Dwyer CR**, **Russell RP**, **Weinreb JH**, **Alaee F**, **Beitzel K**, **McCarthy MB**, **Cote MP**, **Mazzocca AD.** The enthesis: a review of the tendon-to-bone insertion. *Muscles Ligaments Tendons J* 4: 333–342, 2014.
13. **Elmentaite R**, **Kumasaka N**, **Roberts K**, **Fleming A**, **Dann E**, **King HW**, **et al.** Cells of the human intestinal tract mapped across space and time. *Nature* 597: 250–255, 2021. doi:10.1038/s41586-021-03852-1.

Downloaded from journals.physiology.org/journal/ajpcell (090.211.155.175) on May 11, 2026.

14. **Lake BB**, **Menon R**, **Winfree S**, **Hu Q**, **Melo Ferreira R**, **Kalhor K**, **et al.** An atlas of healthy and injured cell states and niches in the human kidney. *Nature* 619: 585–594, 2023.
15. **Mimpen JY**, **Baldwin MJ**, **Paul C**, **Ramos-Mucci L**, **Kurjan A**, **Cohen CJ**, **Sharma S**, **Chevalier Florquin MSN**, **Hulley PA**, **McMaster J**, **Titchener A**, **Martin A**, **Costa ML**, **Gwilym SE**, **Cribbs AP**, **Snelling SJB.** Exploring cellular changes in ruptured human quadriceps tendons at single-cell resolution (Preprint). *bioRxiv*, 2024. doi:10.1101/2024.09.06.611599.
16. **Mimpen JY**, **Ramos-Mucci L**, **Paul C**, **Kurjan A**, **Hulley PA**, **Ikwuanusi CT**, **Cohen CJ**, **Gwilym SE**, **Baldwin MJ**, **Cribbs AP**, **Snelling SJB.** Single nucleus and spatial transcriptomic profiling of healthy human hamstring tendon. *FASEB J* 38: e23629, 2024. doi:10.1096/fj.202300601RRR.
17. **Kendal AR**, **Layton T**, **Al-Mossawi H**, **Appleton L**, **Dakin S**, **Brown R**, **Loizou C**, **Rogers M**, **Sharp R**, **Carr A.** Multi-omic single cell analysis resolves novel stromal cell populations in healthy and diseased human tendon. *Sci Rep* 10: 13939, 2020. doi:10.1038/s41598-020-70786-5.
18. **Akbar M**, **MacDonald L**, **Crowe LAN**, **Carlberg K**, **Kurowska-Stolarska M**, **Ståhl PL**, **Snelling SJB**, **McInnes IB**, **Millar NL.** Single cell and spatial transcriptomics in human tendon disease indicate dysregulated immune homeostasis. *Ann Rheum Dis* 80: 1494–1497, 2021. doi:10.1136/annrheumdis-2021-220256.
19. **Fang F**, **Xiao Y**, **Zelzer E**, **Leong KW**, **Thomopoulos S.** A mineralizing pool of Gli1-expressing progenitors builds the tendon enthesis and demonstrates therapeutic potential. *Cell Stem Cell* 29: 1669–1684.e6, 2022 [Erratum in *Cell Stem Cell* 32: 1792, 2025]. doi:10.1016/j.stem.2022.11.007.
20. **Yan R**, **Zhang H**, **Ma Y**, **Lin R**, **Zhou B**, **Zhang T**, **Fan C**, **Zhang Y**, **Wang Z**, **Fang T**, **Yin Z**, **Cai Y**, **Ouyang H**, **Chen X.** Discovery of muscle-tendon progenitor subpopulation in human myotendinous junction at single-cell resolution. *Research (Wash DC)* 2022: 9760390, 2022. doi:10.34133/2022/9760390.
21. **Zhang T**, **Wan L**, **Xiao H**, **Wang L**, **Hu J**, **Lu H.** Single-cell RNA sequencing reveals cellular and molecular heterogeneity in fibrocartilaginous enthesis formation. *eLife* 12: e85873, 2023. doi:10.7554/eLife.85873.
22. **Fu W**, **Yang R**, **Li J.** Single-cell and spatial transcriptomics reveal changes in cell heterogeneity during progression of human tendinopathy. *BMC Biol* 21: 132, 2023. doi:10.1186/s12915-023-01613-2.
23. **Kurjan A**, **Mimpen JY**, **Ramos-Mucci L**, **Aksu AC**, **Buckley CD**, **Cribbs AP**, **Baldwin MJ**, **Snelling SJB.** Cellular and molecular landscapes of human tendons across the lifespan revealed by spatial and single-cell transcriptomics (Preprint). *bioRxiv*, 2025. doi:10.1101/2025.06.19.660575.
24. **Møbjerg A**, **Steffen D**, **Schjerling P**, **Jakobsen JR**, **Jokipii-Utzon A**, **Batiuk MY**, **Khodosevich K**, **Krogsgaard MR**, **Izzi V**, **Mackey AL**, **Kjaer M**, **Yeung C-YC.** Spatially distinct ECM-producing fibroblasts and myonuclei orchestrate early adaptation to mechanical loading in the human muscle-tendon unit. *Am J Physiol Cell Physiol* 329: C1775–C1791, 2025. doi:10.1152/ajpcell.00700.2025.
25. **Mimpen JY**, **Baldwin MJ**, **Paul C**, **Ramos-Mucci L**, **Kurjan A**, **Cohen CJ**, **Sharma S**, **Chevalier Florquin MSN**, **Hulley PA**, **McMaster J**, **Titchener A**, **Martin A**, **Costa ML**, **Gwilym SE**, **Cribbs AP**, **Snelling SJB.** Exploring cellular changes in ruptured human quadriceps tendons at single-cell resolution. *J Physiol* 603: 4535–4554, 2025. doi:10.1113/JP287812.
26. **De Micheli AJ**, **Swanson JB**, **Disser NP**, **Martinez LM**, **Walker NR**, **Oliver DJ**, **Cosgrove BD**, **Mendias CL.** Single-cell transcriptomic analysis identifies extensive heterogeneity in the cellular composition of mouse Achilles tendons. *Am J Physiol Cell Physiol* 319: C885–C894, 2020. doi:10.1152/ajpcell.00372.2020.
27. **Mimpen JY**, **Paul C**, **Ramos-Mucci L**, **Tendon Seed Network**, **Cribbs AP**, **Baldwin MJ**, **Snelling SJB.** SOP for snap-freezing tissues. Protocols.io, 2022. doi:10.17504/protocols.io.b2tqqemw.
28. **Mimpen JY**, **Paul C**, **Tendon Seed Network**, **Cribbs AP**, **Snelling SJB.** *Nuclei isolation from snap-frozen tendon tissue for single nucleus RNA Sequencing*. Protocols.io, 2021. doi:10.17504/protocols.io.bc6xizfn.
29. **Heumos L**, **Schaar AC**, **Lance C**, **Litinetskaya A**, **Drost F**, **Zappia L**, **et al.** Best practices for single-cell analysis across modalities. *Nat Rev Genet* 24: 550–572, 2023. doi:10.1038/s41576-023-00586-w.
30. **Amezquita RA**, **Lun ATL**, **Becht E**, **Carey VJ**, **Carpp LN**, **Geistlinger L**, **Marini F**, **Rue-Albrecht K**, **Risso D**, **Soneson C**, **Waldron L**, **Pagès H**, **Smith ML**, **Huber W**, **Morgan M**, **Gottardo R**, **Hicks SC.** Orchestrating single-cell analysis with Bioconductor. *Nat Methods* 17: 137–145, 2020 [Erratum in *Nat Methods* 17: 242, 2020]. doi:10.1038/s41592-019-0654-x.
31. **Hao Y**, **Hao S**, **Andersen-Nissen E**, **Mauck WM**, **Zheng S**, **Butler A**, **Lee MJ**, **Wilk AJ**, **Darby C**, **Zager M**, **Hoffman P**, **Stoeckius M**, **Papalexi E**, **Mimitou EP**, **Jain J**, **Srivastava A**, **Stuart T**, **Fleming LM**, **Yeung B**, **Rogers AJ**, **McElrath JM**, **Blish CA**, **Gottardo R**, **Smibert P**, **Satija R.** Integrated analysis of multimodal single-cell data. *Cell* 184: 3573–3587.e29, 2021. doi:10.1016/j.cell.2021.04.048.
32. **Yang S**, **Corbett SE**, **Koga Y**, **Wang Z**, **Johnson WE**, **Yajima M**, **Campbell JD.** Decontamination of ambient RNA in single-cell RNA-seq with DecontX. *Genome Biol* 21: 57, 2020. doi:10.1186/s13059-020-1950-6.
33. **Germain PL**, **Lun A**, **Garcia Meixide C**, **Macnair W**, **Robinson MD.** Doublet identification in single-cell sequencing data using scDblFinder. *F1000Res* 10: 979, 2021. doi:10.12688/f1000research.73600.1.
34. **Young MD**, **Behjati S.** SoupX removes ambient RNA contamination from droplet-based single-cell RNA sequencing data. *Gigascience* 9: giaa151, 2020. doi:10.1093/gigascience/giaa151.
35. **Gayoso A**, **Lopez R**, **Xing G**, **Boyeau P**, **Valiollah Pour Amiri V**, **Hong J**, **Wu K**, **Jayasuriya M**, **Mehlman E**, **Langevin M**, **Liu Y**, **Samaran J**, **Misrachi G**, **Nazaret A**, **Clivio O**, **Xu C**, **Ashuach T**, **Gabitto M**, **Lotfollahi M**, **Svensson V**, **da Veiga Beltrame E**, **Kleshchevnikov V**, **Talavera-López C**, **Pachter L**, **Theis FJ**, **Streets A**, **Jordan MI**, **Regier J**, **Yosef N.** A Python library for probabilistic analysis of single-cell omics data. *Nat Biotechnol* 40: 163–166, 2022. doi:10.1038/s41587-021-01206-w.
36. **Korsunsky I**, **Millard N**, **Fan J**, **Slowikowski K**, **Zhang F**, **Wei K**, **Baglaenko Y**, **Brenner M**, **Loh P-R**, **Raychaudhuri S.** Fast, sensitive and accurate integration of single-cell data with Harmony. *Nat Methods* 16: 1289–1296, 2019. doi:10.1038/s41592-019-0619-0.
37. **Zappia L**, **Oshlack A.** Clustering trees: a visualization for evaluating clusterings at multiple resolutions. *GigaScience* 7: giy083, 2018. doi:10.1093/gigascience/giy083.
38. **Blanco-Carmona E.** Generating publication ready visualizations for Single Cell transcriptomics using SCpubr (Preprint). *bioRxiv*, 2022. doi:10.1101/2022.02.28.482303.
39. **Dann E**, **Henderson NC**, **Teichmann SA**, **Morgan MD**, **Marioni JC.** Differential abundance testing on single-cell data using k-nearest neighbor graphs. *Nat Biotechnol* 40: 245–253, 2022. doi:10.1038/s41587-021-01033-z.
40. **Love MI**, **Huber W**, **Anders S.** Moderated estimation of fold change and dispersion for RNA-seq data with DESeq2. *Genome Biol* 15: 550, 2014. doi:10.1186/s13059-014-0550-8.
41. **Yu G**, **Wang L-G**, **Han Y**, **He Q-Y.** clusterProfiler: an R package for comparing biological themes among gene clusters. *OMICS* 16: 284–287, 2012. doi:10.1089/omi.2011.0118.
42. **Dimitrov D**, **Türei D**, **Garrido-Rodriguez M**, **Burmedi PL**, **Nagai JS**, **Boys C**, **Ramirez Flores RO**, **Kim H**, **Szalai B**, **Costa IG**, **Valdeolivas A**, **Dugourd A**, **Saez-Rodriguez J.** Comparison of methods and resources for cell-cell communication inference from single-cell RNA-Seq data. *Nat Commun* 13: 3224, 2022. doi:10.1038/s41467-022-30755-0.
43. **Nagai JS**, **Leimkühler NB**, **Schaub MT**, **Schneider RK**, **Costa IG.** CrossTalkeR: analysis and visualization of ligand–receptorne tworks. *Bioinformatics* 37: 4263–4265, 2021. doi:10.1093/bioinformatics/btab370.
44. **Bravo González-Blas C**, **De Winter S**, **Hulselmans G**, **Hecker N**, **Matetovici I**, **Christiaens V**, **Poovathingal S**, **Wouters J**, **Aibar S**, **Aerts S.** SCENIC+: single-cell multiomic inference of enhancers and gene regulatory networks. *Nat Methods* 20: 1355–1367, 2023. doi:10.1038/s41592-023-01938-4.
45. **Zhang Y**, **Zhang L**, **Lin X-h**, **Li Z-M**, **Zhang Q-y** Knockdown of IRF3 inhibits extracellular matrix expression in keloid fibroblasts. *Biomed Pharmacother* 88: 1064–1068, 2017. doi:10.1016/j.biopha.2017.01.142.
46. **Lazure F**, **Blackburn DM**, **Corchado AH**, **Sahinyan K**, **Karam N**, **Sharanek A**, **Nguyen D**, **Lepper C**, **Najafabadi HS**, **Perkins TJ**, **Jahani-Asl A**, **Soleimani VD.** Myf6/MRF4 is a myogenic niche regulator required for the maintenance of the muscle stem cell pool. *EMBO Rep* 21: e49499, 2020. doi:10.15252/embr.201949499.

Downloaded from journals.physiology.org/journal/ajpcell (090.211.155.175) on May 11, 2026.

47. **Kurowska-Stolarska M**, **Alivernini S.** Synovial tissue macrophages in joint homeostasis, rheumatoid arthritis and disease remission. *Nat Rev Rheumatol* 18: 384–397, 2022. doi:10.1038/s41584-022-00790-8.
48. **Karlsen A**, **Yeung C-YC**, **Schjerling P**, **Denz L**, **Hoegsbjerg C**, **Jakobsen JR**, **Krogsgaard MR**, **Koch M**, **Schiaffino S**, **Kjaer M**, **Mackey AL.** Distinct myofibre domains of the human myotendinous junction revealed by single-nucleus RNA sequencing. *J Cell Sci* 136: jcs260913, 2023. doi:10.1242/jcs.260913.
49. **Asano Y**, **Trojanowska M.** Fli1 represses transcription of the human α2(I) collagen gene by recruitment of the HDAC1/p300 complex. *PLoS One* 8: e74930, 2013. doi:10.1371/journal.pone.0074930.
50. **Dakin SG**, **Newton J**, **Martinez FO**, **Hedley R**, **Gwilym S**, **Jones N**, **Reid HAB**, **Wood S**, **Wells G**, **Appleton L**, **Wheway K**, **Watkins B**, **Carr AJ.** Chronic inflammation is a feature of Achilles tendinopathy and rupture. *Br J Sports Med* 52: 359–367, 2018. doi:10.1136/bjsports-2017-098161.
51. **Amani V**, **Riemondy KA**, **Fu R**, **Griesinger AM**, **Grimaldo E**, **De Sousa GR**, **Gilani A**, **Hemenway M**, **Foreman NK**, **Donson AM**, **Willard N.** Integration of single-nuclei RNA-sequencing, spatial transcriptomics and histochemistry defines the complex microenvironment of NF1-associated plexiform neurofibromas. *Acta Neuropathol Commun* 11: 158, 2023. doi:10.1186/s40478-023-01639-1.
52. **Kedlian VR**, **Wang Y**, **Liu T**, **Chen X**, **Bolt L**, **Tudor C**, **et al.** Human skeletal muscle aging atlas. *Nat Aging* 4: 727–744, 2024. doi:10.1038/s43587-024-00613-3.
53. **Tadros AS**, **Huang BK**, **Pathria MN.** Muscle-tendon-enthesis unit. *Semin Musculoskelet Radiol* 22: 263–274, 2018. doi:10.1055/s-0038-1641570.
54. **Shamrock AG**, **Dreyer MA**, **Varacallo MA.** *Achilles Tendon Rupture*. StatPearls Publishing, 2025.
55. **Gao Y**, **Li J**, **Cheng W**, **Diao T**, **Liu H**, **Bo Y**, **Liu C**, **Zhou W**, **Chen M**, **Zhang Y**, **Liu Z**, **Han W**, **Chen R**, **Peng J**, **Zhu L**, **Hou W**, **Zhang Z.** Cross-tissue human fibroblast atlas reveals myofibroblast subtypes with distinct roles in immune modulation. *Cancer Cell* 42: 1764–1783.e10, 2024. doi:10.1016/j.ccell.2024.08.020.
56. **Buechler MB**, **Pradhan RN**, **Krishnamurty AT**, **Cox C**, **Calviello AK**, **Wang AW**, **Yang YA**, **Tam L**, **Caothien R**, **Roose-Girma M**, **Modrusan Z**, **Arron JR**, **Bourgon R**, **Müller S**, **Turley SJ.** Cross-tissue organization of the fibroblast lineage. *Nature* 593: 575–579, 2021. doi:10.1038/s41586-021-03549-5.
57. **Smith MH**, **Gao VR**, **Periyakoil PK**, **Kochen A**, **DiCarlo EF**, **Goodman SM**, **Norman TM**, **Donlin LT**, **Leslie CS**, **Rudensky AY.** Drivers of heterogeneity in synovial fibroblasts in rheumatoid arthritis. *Nat Immunol* 24: 1200–1210, 2023. doi:10.1038/s41590-023-01527-9.
58. **Rees SG**, **Davies JR**, **Tudor D**, **Flannery CR**, **Hughes CE**, **Dent CM**, **Caterson B.** Immunolocalisation and expression of proteoglycan 4 (cartilage superficial zone proteoglycan) in tendon. *Matrix Biol* 21: 593–602, 2002. doi:10.1016/s0945-053x(02)00056-2.
59. **Rhee DK**, **Marcelino J**, **Baker M**, **Gong Y**, **Smits P**, **Lefebvre V**, **Jay GD**, **Stewart M**, **Wang H**, **Warman ML**, **Carpten JD.** The secreted glycoprotein lubricin protects cartilage surfaces and inhibits synovial cell overgrowth. *J Clin Invest* 115: 622–631, 2005. doi:10.1172/JCI200522263.
60. **Li H**, **Jiang X**, **Xiao Y**, **Zhang Y**, **Zhang W**, **Doherty M**, **Nestor J**, **Li C**, **Ye J**, **Sha T**, **Lyu H**, **Wei J**, **Zeng C**, **Lei G.** Combining single-cell RNA sequencing and population-based studies reveals hand osteoarthritis-associated chondrocyte subpopulations and pathways. *Bone Res* 11: 58, 2023. doi:10.1038/s41413-023-00292-7.
61. **Waggett AD**, **Ralphs JR**, **Kwan AP**, **Woodnutt D**, **Benjamin M.** Characterization of collagens and proteoglycans at the insertion of the human Achilles tendon. *Matrix Biol* 16: 457–470, 1998. doi:10.1016/s0945-053x(98)90017-8.
62. **Raleigh SM**, **van der Merwe L**, **Ribbans WJ**, **Smith RKW**, **Schwellnus MP**, **Collins M.** Variants within the MMP3 gene are associated with Achilles tendinopathy: possible interaction with the COL5A1 gene. *Br J Sports Med* 43: 514–520, 2009. doi:10.1136/bjsm.2008.053892.

Downloaded from journals.physiology.org/journal/ajpcell (090.211.155.175) on May 11, 2026.